Journal of Alloys and Compounds 1037 (2025) 182315

Contents lists available at ScienceDirect

Journal of Alloys and Compounds

journal homepage: www.elsevier.com/locate/jalcom

Microstructural effects of thermal annealing in GaInNAsSb epitaxial layers

M. Gabás [a,*], A. Landa [b], J. Santiso [c], I. Lombardero [a,d], I. García [a], N. Miyashita [e,f], Y. Okada [e], P.F. Palacios [a], C. Algora [a]

[a] Instituto de Energía Solar, Universidad Politécnica de Madrid, Madrid 28040, Spain
[b] Instituto de Ciencia de Materiales de Madrid (ICMM), CSIC, Cantoblanco, Madrid 28049, Spain
[c] Instituto Catalán de Nanociencia y Nanotecnología (ICN2), CSIC & BIST, Campus UAB, Bellaterra, Barcelona, Spain
[d] GreenPowerMonitor, a DNV Company, Madrid 28016, Spain
[e] Research Center for Advanced Science and Technology (RCAST), The University of Tokyo, 4-6-1 Komaba, Meguro-ku, Tokyo 13-8904, Japan
[f] Department of Engineering Science, The University of Electro-Communications, 1-5-1 Chofu, Tokyo 182-8585, Japan

ARTICLE INFO

Keywords:
GaInNAsSb
Dilute nitride
Annealing
Lattice-matched
Microstructure

ABSTRACT

A set of dilute nitride GaInNAsSb epitaxial layers, some of them submitted to a thermal treatment, has been studied in this work in order to elucidate the microstructural changes induced by annealing. Two semiconductor structures consisting in a GaInNAsSb layer with two different thicknesses, 0.2 and 1 µm, sandwiched between GaAs layers, were grown on GaAs substrates. Three pieces of each structure were studied: one was left as-grown, another one was submitted to a rapid thermal annealing (RTA), and the third one to a longer annealing in a Metal Organic Vapor Phase Epitaxy (MOVPE) reactor. The objective was to compare the GaInNAsSb layer microstructure before and after each thermal treatment, as a function of the dilute nitride layer thickness. The composition profile of the samples and their variations with annealing have been determined using secondary ion mass spectrometry. X-ray diffraction techniques have been used to explore each layer crystalline quality, the lattice mismatch, and the strain. High resolution transmission electron microscopy tools have allowed to establish a quantitative comparison among the samples in terms of misfit dislocations density. Our results indicate that the effect that each annealing has on the microstructure of these GaInNAsSb layers is dependent on the initial state of the as-grown samples. RTA has a limited effect on these layers, while the MOVPE annealing induces noticeable changes in its microstructure.

1. Introduction

Since its development from the GaAs matrix in the 1990s, dilute nitrides (DN) have drawn the attention of both, the material scientists community and the optoelectronic industry, because of their unique physical properties and potential device applications [1–3]. The partial substitution of arsenic with nitrogen atoms, even for concentrations as small as 1 % at., giving rise to the ternary compound GaNAs, is accompanied by a lattice constant reduction and, a modification of the electronic structure (band gap reduction, conduction band splitting), and, as a consequence, of the optoelectronic properties (such as drastic deterioration of photoluminescence, as well as absorption redshift) [4–6]. The main advantage of DN is the bandgap tunability by controlling N incorporation into the GaAs crystalline lattice. The inclusion of other elements, such as In and Sb in adequate amounts, allows for the lattice matched growth of epitaxial DN layers on GaAs and Ge substrates. Therefore, DN have reached an outstanding position as candidates for their incorporation in a wide variety of optoelectronic devices, namely, lasers [7,8], heterojunction bipolar transistors [9,10], near infrared photodetectors [11–14], photoconductive switches [15,16], and in high efficiency multijunction solar cells [17–20].

The growth of epitaxial DN layers has been accomplished by Metal Organic Vapor Phase Epitaxy (MOVPE) [21,22] and Molecular Beam Epitaxy (MBE) [23,24]. Concerning the former one, MOVPE growth of these materials is a difficult task for thin film growers, due to the large miscibility gap between arsenides and nitrides, the unintentional C and H doping, and the formation of a large variety of N-related defects. Conversely, MBE has demonstrated a precise control of the DN layer composition and its crystallinity, and besides, it guarantees lower background carrier densities [25,26]. However, its reduced throughput is burdening the incorporation of these materials in the optoelectronic industry.

* Corresponding author.
E-mail address: mercedes.gabas@upm.es (M. Gabás).

https://doi.org/10.1016/j.jallcom.2025.182315
Received 11 February 2025; Received in revised form 21 May 2025; Accepted 16 July 2025
Available online 17 July 2025
0925-8388/© 2025 The Authors. Published by Elsevier B.V. This is an open access article under the CC BY-NC-ND license (http://creativecommons.org/licenses/by-nc-nd/4.0/).

DN compositions range from ternary (GaNAs), quaternary (GaInNAs, GaNAsSb) and quinary (GaInNAsSb) compounds. Among this wide palette, the corresponding ones to a bandgap value around 1 eV, or even smaller, are those preferred for photovoltaic applications [27], and 3D sensing through vertical cavity surface emitting lasers (VCSEL) [28]. In particular, the quinary compound GaInNAsSb has demonstrated its suitability as the bottom subcell of a multijunction solar cell exhibiting an efficiency of 43.5 % at 925 suns [29], and its active role in VCSELs including DN quantum wells [30].

Normally, the as-grown DN material quality needs to improve to meet the requirements of potential applications, and the most extended way to achieve this improvement is to submit the DN layer to a rapid thermal annealing (RTA), no matter the epitaxial growth method used, nor the DN layer composition [31–34]. Notwithstanding this mostly accepted post-growth RTA treatment, there is not a widely accepted recipe for the optimal annealing temperature/time/process gas, and very often, it even depends on the composition of the DN layer and also on the application it has been grown for [35–37]. On the other side, the fabrication of optoelectronic devices including this material implies the growth of a multilayer structure, for example a multijunction solar cell, usually in a MOVPE reactor. In such conditions, the DN layer will suffer and additional thermal load, namely, a MOVPE annealing, during the growth of any semiconductor layer on top of the DN layer. There are very few works dealing with the effects of the reactor environment/temperature conditions during the growth of the semiconductor layers necessary to complete the semiconductor device on top of a DN layer [18,38,39]. Besides, most of the published works are devoted to the macroscopic alterations affecting the DN optical and electronic properties after annealing [24,33,40,41], and few works are focused on the microstructural changes of the DN layer [39,42–45].

Accordingly, in this work we have focused our efforts on the study of MBE-grown GaInAsNSb layers with two different thicknesses, submitted to either a RTA or a MOVPE annealing. Our goal is to get a deeper insight on the effects that these two types of annealing have on the DN layer crystalline structure. For such purpose, we have correlated structural and microstructural features, with direct measurements of composition profiles, by means of three different characterization techniques, Secondary Ion Mass Spectrometry (SIMS), X-Ray Diffraction (XRD), and Transmission Electron Microscopy (TEM).

2. Experimental

2.1. Epitaxial growth

The GaInNAsSb DN layers were grown on 5 cm (2 in.) semi-insulating GaAs (001) substrates by means of radio frequency-plasma molecular beam epitaxy (RF-MBE) [46,47]. Knudsen cells were used for the Ga and In evaporation, while dimeric As_2 and monomeric Sb fluxes (2×10^{-5} Torr and 1×10^{-8} Torr, respectively) were supplied by valved cracker cells. Epitaxial growth was started with the removal of GaAs native oxidation layer on top of the GaAs substrates at ~600 °C. Then, the temperature was set at 570 °C for the growth of the GaAs buffer layer, and further decreased to 480 °C for the growth of the dilute nitride GaInNAsSb layer. The semiconductor structure was finished by a 50 nm thick GaAs cap layer, for which temperature was raised up to 570 °C. The growth of all layers was performed at the rate of 1.0 µm/h. The multilayer structure of the grown samples is thus from top to bottom, GaAs cap layer/DN layer/GaAs buffer layer/GaAs substrate (Fig. 1). The dilute nitride layer thicknesses (green layer in Fig. 1 left) were targeted to be 0.2 and 1 µm, in such way, two different multilayer structures were grown.

2.2. Annealing

After the growth of both multilayer epistructures, they were cut in pieces. One of them was remained as the as-grown sample while two other pieces were submitted to different annealing procedures. One of them suffered a rapid thermal annealing (RTA) under N_2 gas flow at 750 °C for 5 min, according to the optimization work made by Miyashita and Okada in [26]. The other piece was submitted to a longer annealing in a AIX200/4 MOVPE reactor. The objective of this annealing is to know the effects that the thermal load of the MOVPE growth of the rest of the semiconductor device structure would have on the MBE grown DN bottom subcell properties. The MOVPE annealing lasts more than one hour and it consists of several temperature steps (ranging from 550 to 675 °C) under H_2/AsH_3 gas flow, mimicking the thermal load corresponding to the growth of the middle (GaInAs) and the top (GaInP) subcells in a multijunction solar cell structure, together with the corresponding tunnel junctions and window layers [18]. This hybrid MOVPE+MBE growth for 3 J and 4 J solar cells has been proposed as a way to take advantage of the high throughput of MOVPE while maintaining the superior DN material quality of MBE [18,39,48,49] Therefore, considering the two as-grown samples and the four annealed ones (two for each thickness), a total of 6 samples have been investigated in this work. Table 1 gathers the nomenclature of the samples, as well as the DN layer thickness and the annealing procedure each sample has been submitted to.

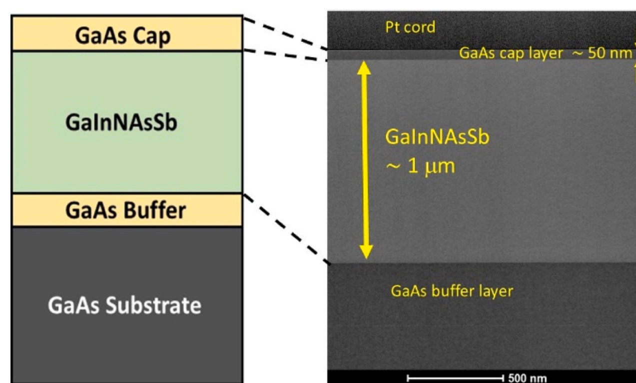

Fig. 1. left, schema (not to scale) of the semiconductor multilayer structure; right, STEM picture of the multilayer structure cross-section corresponding to the as-grown DN_10 sample (see Table 1 for nomenclature identification). DN and GaAs cap layer real thicknesses are indicated in the figure.

Table 1
Nomenclature of the 6 samples studied in this work, according to the DN layer thickness and to the annealing process each sample has been submitted to.

DN layer thickness	AS-GROWN	RTA	MOVPE
0.2 µm	DN_02	DN_R02	DN_M02
1 µm	DN_10	DN_R10	DN_M10

2.3. Characterization methods

An approach to the samples composition profiles has been obtained through SIMS measurements, that have been performed on advanced CAMECA tools at Loughborough Surface Analysis (LSA) Ltd in the United Kingdom. Ion source was Cs^+ operating at 10 keV energy. Secondary ion polarity was positive for N, In and Sb, and negative for H profiles. Beam current and raster size values were adjusted depending on the element profiles. Depth scales were determined by measuring the sputtered crater depths on a Dektak 6 M.

High resolution X-Ray diffraction analysis of the films was made in a Malvern-Panalytical X'Pert MRD diffractometer with CuKα tube and a parabolic mirror with either 2x or 4x Ge(220) monochromators in the incident beam, and a 2D PIXcel array detector. Linear 2θ/ω scans around the 004 GaAs reflection, as well as reciprocal space maps around asymmetric 224 reflections, were measured to assess the crystal quality

of the films, measure the corresponding out-of-plane cell parameters, and to evaluate the degree of in-plane epitaxial strain.

In order to carry out the nanostructural characterization by means of Scanning Transmission Electron Microscopy (STEM) and High Resolution Transmission Electron Microscopy (HRTEM), cross-section samples were prepared using focused ion beam (FIB) milling (at 30 kV and 65–9.4 nA) in a FEI Helios Nanolab 650 Dual Beam microscope, fitted with a Tomahawk FIB at the University of Málaga (Spain), which allows a precise and reliable milling. In these cases, the sample surface was previously protected by a cord of platinum deposited using a gas injection system. STEM and HRTEM images were taken in a FEI Talos F200X, fitted with a 200 KV field emission gun. The high-resolution images have been processed using DigitalMicrograph® software of Gatan Inc.

3. Results

3.1. SIMS

Composition depth profiles measured by SIMS constitute an approximation to the DN layer composition of the samples. First figure in this section (Fig. 2) illustrates the amount of N, In and Sb incorporated to the DN layer in the as-grown samples, with thickness 0.2 µm (DN_02) and 1.0 µm (DN_10). As it is evident in these figures, in spite of the same nominal MBE growth routine for the two multilayer structures, there are differences in the contents of these three elements between the as-grown samples, especially for Sb, for which the concentration of Sb is 2.5 times higher in the DN_10 sample. It is also remarkable the fact that the Sb element profile is not flat for the DN_10 sample, but increases from the bottom of the layer to the surface of the sample. The reason for this anomalous Sb profile is that As_2 flux decreased to 1×10^{-5} Torr during the DN layer growth, facilitating thus the incorporation of Sb in the GaAs matrix. On the other hand, slight growth temperature differences for the DN_02 and DN_10 samples could be behind the differences in N and In concentrations [50]. The concentration of In varies very little between DN_02 and DN_10, with an excess of 0.3 x 10^{21} atoms/cm^3 for DN_02. That is, the amount of In is a bit higher for the thinnest sample, 8.9 % at. (DN_02) vs. 7.9 % at. (DN_10). Both values are very similar to the targeted In content (9 % at. as it is deduced from [47]). On the contrary, for N, the difference reaches an excess of 20 % for DN_10. It is observed that Sb experiences a delay of about 10 nm in its incorporation into the DN layer compared to N and In. This is because the Sb flux for these samples was small (1×10^{-8} Torr of beam equivalent pressure) [50], and therefore, more difficult to get stabilized. As a conclusion, there are subtle differences in the composition of the dilute nitride layers, that may be considered more relevant for the Sb concentration.

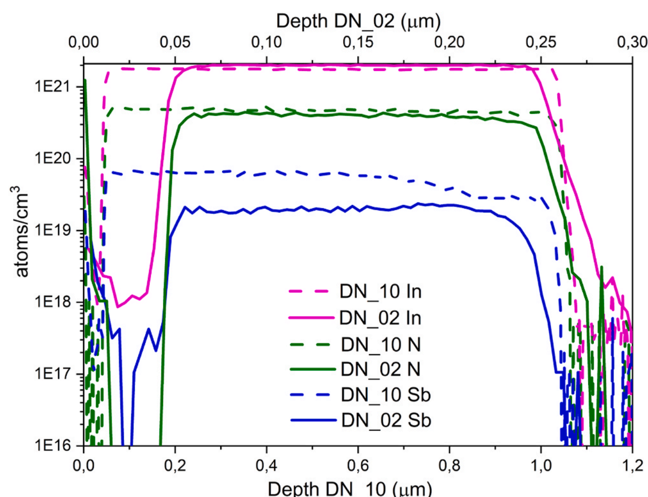

Fig. 2. Graphic showing the content of In (magenta lines), N (green lines) and Sb (blue lines) for the as-grown samples. Solid lines are for the 0.2 µm thick sample (DN_02), while dashed lines are for the 1 µm thick sample (DN_10). Y-scale is common for both sets of data. Top X-scale is for the 0.2 µm sample while bottom X-scale correspond to the 1 µm sample.

RTA treatment does not change the DN layer composition. In the supplementary material file, we show the In, N and Sb profiles for the as-grown 1 µm thick sample, DN_10, and for the RTA annealed one, DN_R10 (Figure S1). As it is evident in the Figure S1, no changes nor in these elements amount, nor in the profile shape, have been detected in the SIMS measurements. Therefore, composition of the RTA annealed samples should be the same than for the as-grown samples.

On the contrary, MOVPE annealing induces some compositional changes that we are going to describe here. First of all, a non-negligible amount of H (around 10^{18} atoms/cm^3) has been detected for the MOVPE annealed samples (DN_M02 and DN_M10) in the DN layer. It is worth mentioning here that the H profile was measured also for the as-grown and the RTA samples, but the amount detected was under the SIMS set-up detection limit. As depicted in Fig. 3, the H profile shape is very similar for DN_M02 and DN_M10 samples, irrespective of the DN layer thickness, slightly decreasing from outer to inner parts along the DN layer thickness. The incorporation of H into a DN layer after MOVPE annealing was also noticed in a previous work for similar samples [39], though in that work annealing time was just 10 min. In our work, the MOVPE annealing time is longer than one hour, in spite of which, the concentration of hydrogen detected in the GaInNAsSb layer is on the same order of magnitude (around 10^{18} atoms/cm^3, see Table 3) than in [39].

It can be thus concluded that H incorporation from the H_2 flux and the AsH_3 pyrolysis into the DN layer is the main effect of the MOVPE annealing on the DN composition.

In Fig. 4, the In (top), Sb (middle) and N (bottom) profiles for both, the as grown and the MOVPE annealed samples, are shown, and the mean values for these elements concentration are gathered in Table 2. No differences in the In amount have been detected between the as-grown and the MOVPE annealed samples. The only difference we see for the 1 µm sample is a small shift at the onset of the MOVPE profile (right part in the Fig. 4 right top). It may be indicative of a small thickness decrease for the annealed sample, as compared to DN_10. However, small variations in the SIMS set-up depth calibration cannot be discarded as the origin of this edge shift, since the measurements of the DN_10 and DN_M10 samples were conducted on different days.

A difference in Sb concentration before and after MOVPE annealing is noticed for the 0.2 µm thick samples, where, after annealing, Sb

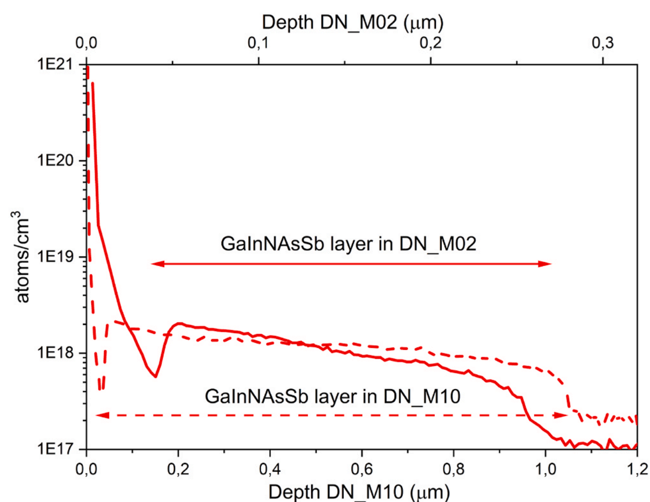

Fig. 3. H profiles for the DN_M02 (solid line) and DN_M10 (dashed line) samples. Horizontal arrows estimate the DN layer thickness for both samples.

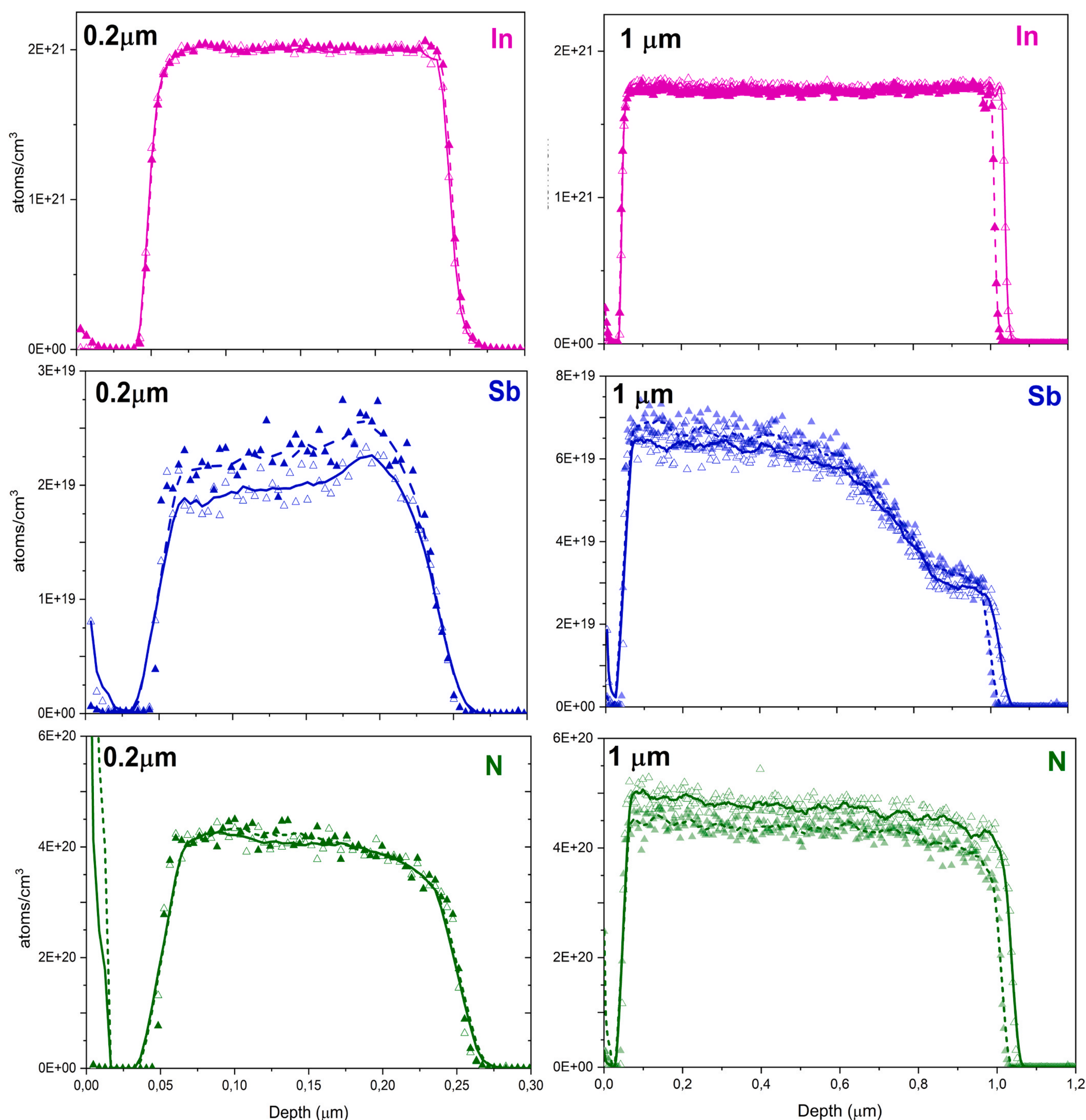

Fig. 4. left, In, Sb and N concentration profiles for the 0.2 μm thick samples: DN_02 (solid lines, hollow triangles) and DN_M02 (dashed lines, filled triangles); right, In, Sb and N concentration profiles for the 1.0 μm thick samples: DN_10 (solid lines, hollow triangles) and DN_M10 (dashed lines, filled triangles).

Table 2
estimated concentrations of H, In, N, and Sb elements across the DN layer thickness for the as-grown, and the MOVPE annealed, samples.

	[H] (atoms/ cm^3)	[In] (atoms/ cm^3)	[N] (atoms/ cm^3)	[Sb] (atoms/ cm^3)
DN_02	-	2.0×10^{21}	3.9×10^{20}	1.9×10^{19}
DN_M02	$\sim 10^{18}$	2.0×10^{21}	3.9×10^{20}	2.2×10^{19}
DN_10	-	1.7×10^{21}	4.7×10^{20}	5.2×10^{19}
DN_M10	$\sim 10^{18}$	1.7×10^{21}	4.3×10^{20}	5.6×10^{19}

amount reaches 2.2×10^{19} atoms/cm^3, which is a relative increase of more than 17 %. For the 1 μm thick sample, a slight increase in Sb concentration has also been estimated, though in this case, it is smaller, 7 % as referred to the as-grown sample. Accompanying this Sb concentration increase, a N concentration decrease (8 % relative) has also been detected in the DN_M10 sample (Fig. 4 bottom right). Conversely, no alteration in the N amount has been detected for the DN_M02 sample (Fig. 4 bottom left).

3.2. . XRD

The XRD analysis of the as-grown and annealed samples with

different thickness is shown in Fig. 5. The high-resolution 2θ/ω scans around the 004 reflection of the GaAs substrate show intense peak maxima for the as-grown DN layers at different 2θ angles, corresponding to out-of-plane cell parameters of $c = 5.680$ Å and 5.664 Å for the 0.2 and 1.0 μm thickness, respectively, while the GaAs substrate is $c= 5.653$ Å. The observation of Laue fringes (or Pendellösung oscillations) for the thinner DN_02 layer, corresponding exactly to a 0.2 μm film thickness, is a proof of the high crystal quality of the layer. These oscillations are not observed for the thicker DN_10 film, probably because of the very large thickness of 1.0 μm. Additionally, there are other oscillations of higher 2θ spacing which correspond to a thickness of 50 nm, consistent with the GaAs cap layer thickness, in agreement with the STEM picture shown in Fig. 1 right (the homoepitaxial GaAs buffer layer is not expected to give any signal on the GaAs substrate). The corresponding reciprocal space maps (RSM) (Fig. 5 right) of the 224 reflections show the same value of the GaAs substrate and DN layer Q_x components in the reciprocal space, indicating a perfect in-plane matching of the structures along the [110] in-plane crystallographic direction. The corresponding Q_z components allow to calculate out-of-plane cell parameters of $c = 5.680$ Å and $c = 5.664$ Å, for the 0.2 and 1.0 μm thickness, respectively, in perfect agreement with the measurement of the 004 symmetric reflection, while the in-plane cell parameter is calculated in $a= 5.655$ Å. Both film structures are then distorted to a tetragonal cell to match the GaAs substrate. A closer inspection into the XRD profiles shows that the full width at half maximum (FWHM) of the 004 peak for the 0.2 μm sample is 0.060°, while for the thicker film of 1.0 μm is 0.035° (see Fig. 6). This difference could not be directly related to the film thickness and should come from differences in the crystal quality of the film. The RSM of the 224 reflection for the 0.2 μm layer shows also certain spread along Q_x not observed for the thicker 1.0 μm DN film, pointing in the same direction of the formation of point defects during the DN layer growth. The reason why the 1.0 μm layer does not show such spread may come from the fact that for this sample, the XRD signal has a larger weight from the more external part of the DN layer, which seems to have heal the defects upon film growth.

After the annealing treatments, several changes deserve attention in both, the 004 diffraction profiles, and the 224 RSMs (Fig. 5). RTA has a small effect in the out-of-plane mismatch. For the thinner sample, DN_R02, there is a very small shift in the 004 reflection (Fig. 5 top left), but no change is detected in the 224 RSM, meaning thus that unit cell remains almost equal than before RTA. On the contrary, for the 1 μm thick sample, DN_R10, the increase in the mismatch between GaAs

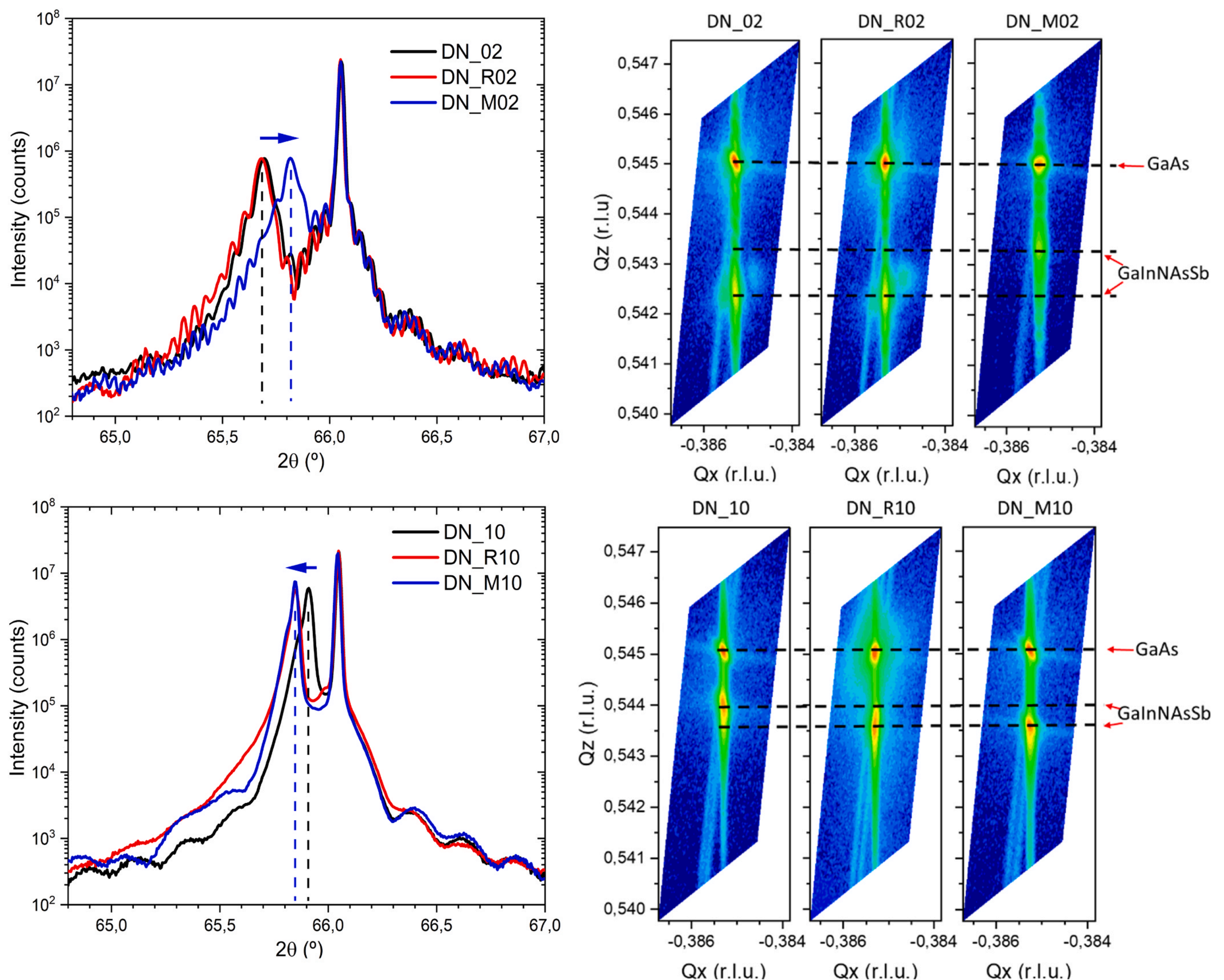

Fig. 5. Left, evolution of the 004 XRD profiles of the GaInNSbAs films from the as deposited state (black lines) and after the different type of annealing, RTA (red lines), and MOVPE (blue lines), for both, 0.2 (top) and 1.0 (bottom) μm thickness DN layers. Small horizontal arrows indicate the evolution of the out-of-plane cell parameter after MOVPE annealing in both graphics. Right, the corresponding 224 reciprocal space maps for both, 0.2 (top) and 1.0 (bottom) μm thickness DN layers. Horizontal dashed lines mark the position along Q_z of the GaAs substrate (upper line) and the GaInNAsSb layers, in this case, before and after the thermal treatments.

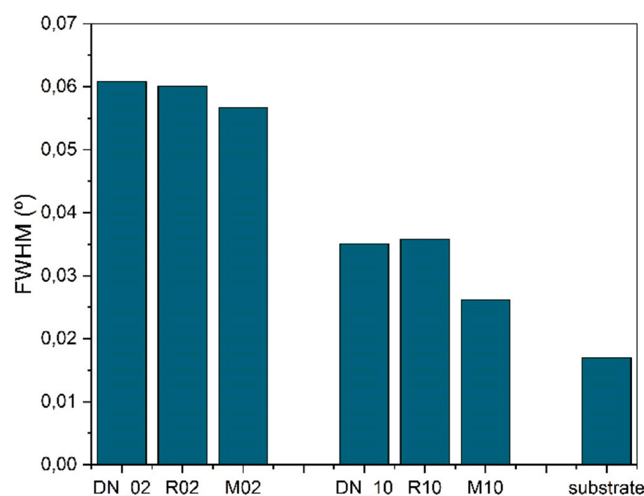

Fig. 6. 004 reflection FWHM of the six DN samples and of the GaAs substrate. The three columns on the left part of the graphic correspond to 0.2 mm samples. The three columns in the middle account for the FWHM of the 1 mm samples. 004 FWHM GaAs substrate is the isolated column on the right.

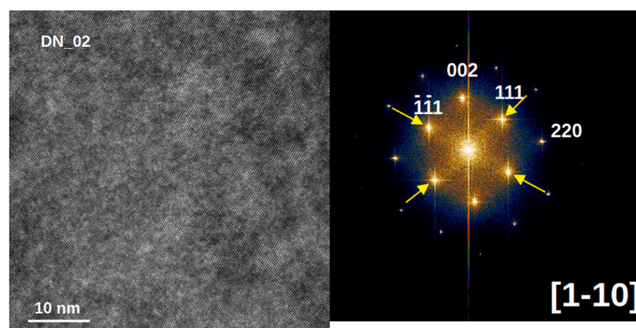

Fig. 7. left, HRTEM image of the as-grown sample DN_02; right, colored FFT from the HRTEM image on the left, the yellow arrows indicate the diffuse intensity observed along the [-111]* reciprocal direction. In the figure on the left, growth direction is from bottom to top.

substrate and DN layer along the growth direction is visible in both, 004 profile and the 224 RSM (Fig. 5 bottom left & right). MOVPE annealing has a different effect in the out-of-plane component depending on the DN layer thickness. For the 0.2 µm thick sample, DN_M02, the thermal treatment reduces the mismatch between the GaAs substrate and the DN layer (see 004 profile and 224 RSM in Fig. 5 top). Conversely, for the 1 µm thick sample, there is an out-of-plane mismatch increase, evident in the 004 profile and in the 224 RSM (Fig. 5 bottom). The in-plane component does not get any alteration after RTA, nor after MOVPE annealing (Fig. 5 right), therefore in-plane strain remains after both thermal treatments, irrespective of DN layer thickness.

Another aspect that deserves attention is the FWHM of the 004 profiles after annealing. There are opposite tendencies after RTA, since for the 0.2 µm sample, there is a small decrease, while for the 1 µm sample, the FWHM increases as compared to that of the as-grown sample (see Fig. 6). After the MOVPE annealing, the same variation occurs, no matter the DN layer thickness, there is a decrease in the FWHM value, more noticeable for the thicker sample, DN_M10.

As a summary, we can conclude from HRXRD measurements that only the out-of-plane component gets affected by thermal treatments, but there are differences depending on the as-grown DN layer thickness. For the thinner samples, RTA has almost no effect on the lattice mismatch between GaAs substrate and DN layer, while MOVPE annealing reduces the mismatch of the DN layer. For the 1 micron samples, both, RTA and MOVPE treatments have a similar effect, an increase in the lattice mismatch along the growth direction.

3.3. TEM

In Fig. 7 left we show a high resolution transmission electron microscopy (HRTEM) cross-section image of the GaInNAsSb layer of sample DN-02. Notice the bright-dark contrast observed all along the image of Fig. 8 7 left. Its fast Fourier transform (FFT) is presented in Figure S2, where besides the reflection maxima indexed in the GaAs structure along the [1−10] direction, we can also see the presence of weak diffuse intensity between the diffracted maxima which seems to be weakly structured along the [111]* and [-1−11]* reciprocal directions. Fig. 7 right is a colored version of Figure S2 in order to highlight this diffuse intensity. For the 1 micron thick sample, DN_10, we have obtained similar images (see Figure S3 in the supplementary material file), and there is also a diffuse scattered intensity along the equivalent [111]* reciprocal directions, even more intense than in DN_02 sample.

In order to check the possible cause for the diffuse intensity shown in Fig. 7 right, we have processed the image from the experimental FFT by selecting the 111 and −1–1–1 reflections, and reconstructing the image only with these reflections by an inverse fast-Fourier transform (IFFT). The resulting image is shown in Fig. 8 top left. It is clear the presence of certain bright-dark structuration of the sample HRTEM contrast. The dark contrast can be due to strain fields in the crystal which can be caused by the presence of dislocations in the crystal lattice [51]. In order to facilitate the visualization of these possible dislocations, we have colored the image (Fig. 8 top right), in such way that the darkest areas of Fig. 8 top left image are now green and the bright areas are yellow. A closer inspection into the greener part of the images allows to distinguish that there are many edge dislocations that are indicated in an enlarged area of the image shown in Fig. 8 bottom right. Notice as well that no dislocation can be found in the yellow areas, i.e., the yellow zones are defect-free crystalline areas. For the sake of comparison between samples, in an attempt to quantify the dislocations density at this local scale, we have quantified the total number of dislocations in Fig. 8 bottom left as 24 (see Table 3).

The explanation for the presence of dislocations in selected zones could be that the yellow areas indicate the core of crystal domains that have grown as crystals along [111] orientation, while the green areas could be explained as the grain boundaries. During the growth of the layers, germinal crystallites formed and grew free of defects until they collapsed against neighbor crystallites giving rise to dislocation riche grain borders. The alignment of these dislocations along rows perpendicular to the [111] direction must be the cause of the diffuse scattering observed in the diffraction pattern along [111]* directions in the reciprocal space.

The same procedure has been applied to the HRTEM image corresponding to the sample DN_10 (Figure S3 in the supplementary material file). The resulting IFFT image is shown in Fig. 9. Again, green zones are those where the crystalline strain is significant. From the dislocations distribution observed in Fig. 9, we cannot infer a clear alignment of dislocations perpendicular to the [111] direction, although the diffuse intensity structuration along the [111]* reciprocal directions is also visible in the diffraction pattern, (see Figure S3 right in the supplementary material file). In this case, a higher number of dislocations, 41, is present. The reason for the higher number of dislocations in DN_10 sample compared to DN_02 sample is not clear at all. It could be related with the different thicknesses of both samples and slightly growth conditions. For example, DN_10 layer is thicker than DN_02 and in some way the layer growth would stimulate the formation of certain type of defects. It is customary to state here that the HRTEM pictures from which these IFFT images have been constructed, extend over about 50 nm of the total DN layer thickness, and that they have been taken in the middle of the DN layer total thickness. Therefore, the amount of dislocations deduced from the IFFT images may not be representative of

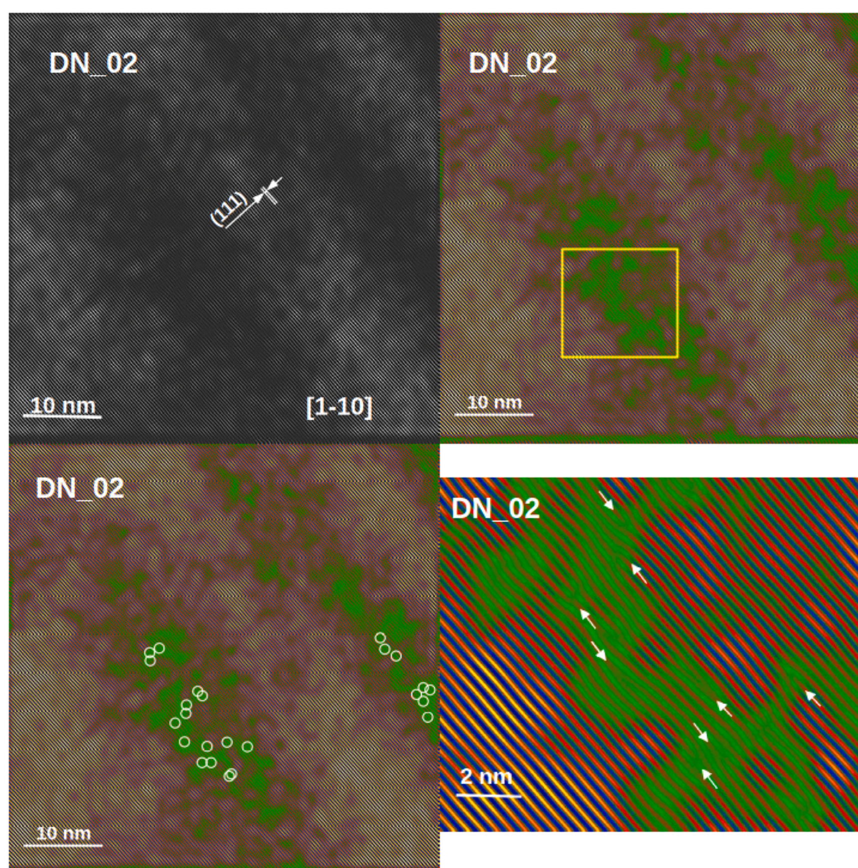

Fig. 8. top left, IFFT image of the as-grown DN-02 sample by filtering the 111 reflections; top right, colored IFFT image of Fig. 8 top left; bottom left, the same as Fig. 8 top right where the dislocations are marked with white circles; bottom right, detail of the area enclosed in the yellow rectangle in Fig. 8 top right, where some of the edge dislocations are indicated with white arrows.

Table 3
quantification of the dislocations found in Fig. 10.

Sample	DN_02	DN_R02	DN_M02	DN_10	DN_R10	DN_M10
n. dislocations	24	22	187	41	29	3

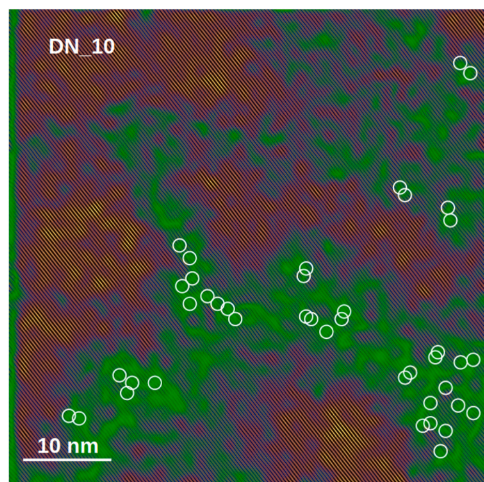

Fig. 9. colored IFFT image of the DN_10 sample. Dislocations are surrounded by white circles. The original HRTEM image is shown in Fig. S4, as well as the FFT picture.

the entire thickness of the layer and may change from the bottom to the top throughout the entire thickness.

After the annealing treatments, RTA and MOVPE, the same procedure has been applied to the DN layer HRTEM pictures taken for the samples DN_R02, DN_R10, DN_M02 and DN_M10 (see Figure S4 in the supplementary material file). In Fig. 10, we show the colored IFFT images of these four samples where the dislocations are surrounded by white circles. The number of dislocations found in the respective IFFT for each sample can be seen in the Table 3. As it has been already seen in the XRD results, the effect of the RTA annealing is dependent on the DN layer thickness. For the 0.2 µm thick layer, there are no apparent changes in the microstructure, and the number of dislocations found for DN_R02 sample is similar to that of DN_02 sample. On the contrary, a small decrease in the dislocations density appears for the DN_R10 sample, as compared to the as-grown sample. Concerning MOVPE annealing, opposite effects are detected for DN_M02 and DN_M10 samples. A notorious increase in the amount of dislocations is evident for the first sample, while an also notorious decrease is noticeable for the 1 µm thick sample.

4. Discussion

First of all, it is worth mentioning here the initial slight differences between both as-grown samples DN_02 and DN_10. The larger In amount in the 0.2 µm layer, as well as the smaller N and Sb concentrations, as compared to the 1 µm layer (see Table 2 in the Section 3.1), tell us about the competition among the precursor fluxes for these three elements. In this case, there was an As flux variation which favored the incorporation of Sb in the DN_10 layer. This compositional difference may be one of the reasons for the relative larger *c*-axis parameter (about 0.3 %) of the

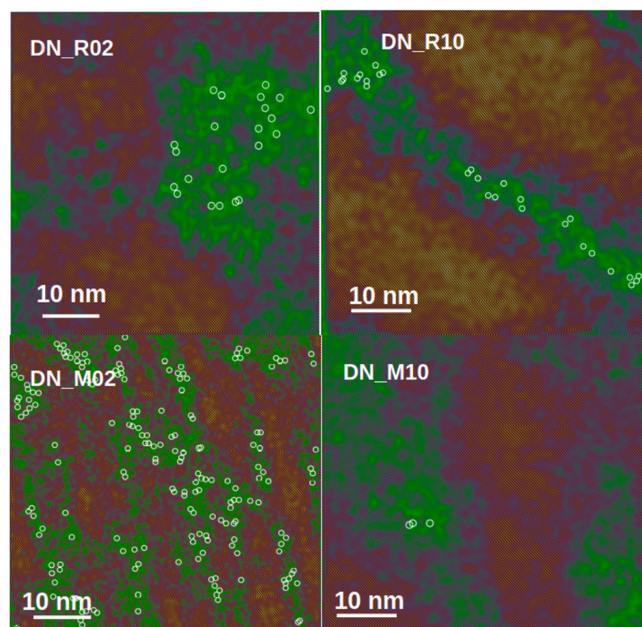

Fig. 10. colored IFFT images of the DN_R02 (top, left), DN_R10 (top right), DN_M02 (bottom left), and DN_M10 (bottom right).

0.2 µm layer compared to the 1 µm layer. Additionally, the formation of point defects related with N during the DN layer growth, cannot be discarded as a possible origin for the out-of-plane differences between the as-grown layers, since it is a well-known fact that N induces the formation of a wide variety of point defects in the GaAs matrix, namely, N_2 substitutional, interstitial N, N split interstitial, etc… [19,52–55]. For the DN_10 layer, the higher deposition growth time may induce a self-annealing that would reduce the average point defect density. The higher FWHM in the 004 reflection profile for the DN-02 sample as compared to that of the DN-10 sample (see Fig. 6), would be a direct consequence of this higher point defect density for the thinner sample. Additionally, the RSM of the 224 reflection shows a spread along Q_x for the DN_02 sample (see Fig. 5 7 right), which is also probably related with this more important point defects abundance. The HRTEM pictures and the IFFT images constructed from the former, also evidence differences between DN_02 and DN_10 samples. A higher amount of edge dislocations has been found for the DN_10 sample, though the reason for such difference remains unknown, and we can only hypothesize on it taking into account that the HRTEM images have been taken at the mid part of the DN layer thickness, which means that in the case of the 0.2 mm thick sample we are less than 100 nm away from the interface with the buffer layer, while for the DN_10 sample the distance is quite higher. Another possible reason may lie in the higher amount of Sb for the DN_10 sample, which may act as an additional source of a different type of point defects increasing the dislocation density.

After the RTA treatment, we have observed no change in the DN layer composition, according to SIMS results. Therefore, the differences in composition pointed out for the as-grown samples, remain identical for DN_R02 and DN_R10. However, local atomic redistributions (which may lead to defect elimination and are undetectable in SIMS profiles) cannot be excluded after this thermal annealing. In such way, the RTA treatment affects in a different way to DN layer depending on its thickness. For the thinner layer, 0.2 µm thick, XRD data show just a very small mismatch increase in the out-of-plane component in the 004 reflection profile, together with a minute FWHM decrease. Accordingly, the density of dislocations detected in the DN_R02 HRTEM image (see Table 3), is very similar to that found for the DN_02 sample. On the other hand, RTA treatment has a clear effect in the DN_R10 004 reflection profile, as well as in the 224 RSM, indicating a lattice mismatch increase in the out-of-plane component for this sample, which is accompanied by a small, but detectable, FWHM increase for the 004 reflection profile (Fig. 6). HRTEM also evidences differences between the as-grown sample, DN_10, and DN_R10, for which a decrease in the number of dislocations has been quantified in Table 3 (Fig. 10 top right). In previous works, the effect of a short annealing in N_2 atmosphere, like our RTA treatment, on GaInNAs layers, was described as a rearrangement of the N bonds, increasing the ratio In-N vs. Ga-N after annealing [34,43,44]. This accommodation of In and N in the GaAs matrix is probably behind the changes in XRD and HRTEM detected for the DN_R10 sample in this work, and it is in agreement also with the SIMS results, since this rearrangement does not imply any compositional change. For the DN_R02 sample however, this annealing does not seems to provide enough energy to the crystal lattice to favor N displacements along the DN layer, probably because of already mentioned higher point defect density in the as-grown 0.2 µm layer, as compared to the 1 µm one.

MOVPE annealing has a clear effect on the DN layers since it promotes the diffusion of H along the entire layer thickness as seen by SIMS (Fig. 3). The amount of H is not dependent on the DN layer thickness and in fact, it seems that there is a solubility limit for this element, since the same profile and H quantity has been reported in previous works [39]. Together with the incorporation of H, the elements N and Sb exhibit variations in their concentrations in the DN layer after MOVPE annealing, though they depend on the DN layer thickness (see Table 2 and Fig. 4). For the thinner layer, DN_M02, N amount does not change as compared to that in DN_02, but Sb experiments an increase which is as high as 17 % relative, and the most probable option is that Sb atoms enter as point defects in the GaAs matrix. Accompanying this change, a diminution in the out-of-plane parameter is evident in the 004 reflection profile and in the 224 RSM (Fig. 5 top), that implies a better lattice match for the DN_M02 sample. Besides, a FWHM decrease in the 004 reflection profile has been noticed for both DN layer thickness (Fig. 6), which could be motivated by a point defect density diminution of defects related to N. The combination of the Sb incorporation and the unit cell compactification could be the reason for the very high increase of the number of dislocations found for this sample (Table 3 and Fig. 10 bottom left). For the DN_M10 sample, there is a smaller Sb incorporation (as compared to the DN_M02 sample) combined with a decrease in the N amount in the DN layer (Table 3 and Fig. 4 right). This N amount diminution is probably associated with a reduction in defect density related to this element. Besides, the 004 reflection profile and the 224 RSM indicate an out-of-plane lattice mismatch increase (Fig. 5 bottom). The combination of these alterations may be behind the drastic decrease in the number of dislocations observed for this sample (Table 3 and Fig. 10 bottom right).

5. Conclusions

A set of six DN GaInNAsSb MBE grown layers with two different thicknesses, 0.2 and 1 µm, have been studied to explore the influence of two different thermal treatments, namely RTA and MOVPE, on the DN microstructure. For such purpose SIMS, XRD and HRTEM techniques have been used. The as-grown samples, DN_02 and DN_10, exhibit slight compositional differences, i.e. variations in the In, N and Sb concentrations. As a consequence, the 0.2 µm thick sample exhibits a higher lattice mismatch. Besides, the 004 profile FWHM is also higher for this sample, which may be related to a higher point defects density. The small differences between these samples also extend to the microstructure revealed in the HRTEM images, with a greater presence of dislocations for the thicker samples.

RTA treatment does not alter the DN layer composition. However, it provokes a lattice mismatch increase for the DN_R10 sample, accompanied by a diminution in the dislocation density. The more probable reason for these changes is the rearrangement of N and In atoms in the GaAs matrix. For the DN_R02 sample, the energy provided during RTA treatment is probably not high enough to induce the same changes than

in DN_R10, and the reason may lie in the higher point defect density suggested by XRD results. As a consequence, for the DN_R02 sample, there is no difference, nor in the XRD, nor in the TEM images, with the as-grown sample.

MOVPE annealing lasts for more than one hour and the combination of time and temperature makes possible to affect in a significant way to both as-grown samples, though there are differences according to DN layer thickness. There are common effects for both layer thicknesses, namely, the H diffusion in the DN layer and a point defect density decrease. The profile and amount for H are similar for both layers. For the 0.2 µm thickness DN layer, a 17 % increase for the Sb amount in the DN layer. This incorporation of Sb is probably accompanied by the rising of new point defects not related with N, and this fact combined with a unit cell compaction, may be responsible for the drastic increase in the dislocations density seen in DN_M02. Conversely, in the DN_M10 sample, there is a small increase for the Sb amount but a decrease for N, in such a way that there could be a compensation between the rising and the elimination of different point defects in the GaAs lattice. As a result, the lattice mismatch increases along the growth direction, being the final consequence a dramatic diminution in the dislocations density.

The effect that thermal treatments have on the DN layer microstructure is strongly dependent on the initial state in the as-grown sample. MOVPE treatment has a deeper effect on the DN layer crystalline structure and microstructure, since it involves alterations in the composition, which are probably related to the appearance/compensation of some kind of point defect within the crystal lattice, and give rise to the alterations observed in XRD and HRTEM.

Declaration of Competing Interest

The authors declare that they have no known competing financial interests or personal relationships that could have appeared to influence the work reported in this paper.

Acknowledgments

This paper has been supported by the Grant PDC2021–120748-I00 funded by MICIU/AEI/ 10.13039/501100011033 and by the European Union Next Generation EU/PRTR, and also by the Universidad Politécnica de Madrid through “Ayudas para la cofinanciación de infraestructuras de I+D+i (Programa Propio)”. Pablo Fernández Palacios acknowledges the grant PRE2021–099669 with financial support from MICIU/AEI /10.13039/501100011033 and from FSE+ . A part of this work was supported by the Incorporated Administrative Agency New Energy and Industrial Technology Development Organization (NEDO), and Ministry of Economy, Trade and Industry (METI), Japan. The authors want to acknowledge the technical support of Rocío Romero and Adolfo Martínez from the Servicios Centrales de Apoyo a la Investigación at the University of Málaga (Spain), during the SEM-FIB and TEM experiments.

Appendix A. Supporting information

Supplementary data associated with this article can be found in the online version at doi:10.1016/j.jallcom.2025.182315.

References

[1] M. Weyers, M. Sato, H. Ando, Red shift of photoluminescence and absorption in dilute GaAsN alloy layers, Jpn. J. Appl. Phys. 31 (1992) L853–L855, https://doi.org/10.1143/JJAP.31.L853.

[2] M. Kondow, K. Uomi, A. Niwa, T. Kitatani, S. Watahiki, Y. Yazawa, GaInNAs: a novel material for long wavelength-range laser diodes with excellent high temperature performance, Jpn. J. Appl. Phys. 35 (1996) 1273–1275, https://doi.org/10.1143/JJAP.35.1273.

[3] D.J. Friedman, J.F. Geisz, S.R. Kurtz, J.M. Olson, 1-eV solar cells with GaInNAs active layer, J. Cryst. Growth 195 (1998) 409–415, https://doi.org/10.1016/S0022-0248(98)00561-2.

[4] W. Shan, K.M. Yu, W. Walukiewicz, J. Wu, J. Ager, E.E. Haller, Band anticrossing in dilute nitrides, J. Phys. Cond. Matter 16 (2004) S3355–S3372.

[5] M. Henini (Ed.), Dilute Nitride Semiconductors, Elsevier Ltd, 2005.

[6] A. Erol (Ed.), “Dilute III-V Nitride Semiconductors and Material Systems: Physics and Technology”, Springer, 2010.

[7] H. Zhao, Y.Q. Xu, H.Q. Ni, S.Y. Zhang, Q. Han, Y. Du, X.H. Yang, R.H. Wu, Z.C. Niu, Post-growth and in situ annealing on GaInNAs(Sb) and their application in 1.55 µm lasers, Semicond. Sci. Technol. 21 (2006) 279–282, https://doi.org/10.1088/0268-1242/21/3/011.

[8] S.F. Yoon, K. Tan, W. Loke, S. Wicaksono, K. Lew, T. Ng, Z. Xu, Y. Sim, A. Stöhr, S. Fedderwitz, M. Weiß, O. Ecin, A. Poloczek, A. Malcoci, D. Jäger, N. Saadsaoud, E. Dogheche, M. Zegaoui, J. Lampin, D. Decoster, C. Tripon-Canseliet, S. Faci, J. Chazelas, J. Gupta and S. McAlister, “Recent progress in dilute nitride-antimonide materials for photonic and electronic applications” at the State-of-the-art program on compound semiconductors 50 (SOTAPOCS 50) - and- processes at the semiconductor solution interface 3. Proc. 215th ECS Meeting, ECS Transactions 19 (2009).

[9] J.C. Harmand, L. Li, R. Mouillet, G. Ungaro, V. Sallet, L. Travers, G. Patriarche, L. Largeau, R. Kudrawiec, G. Sek, J. Misiewicz, GaNAsSb alloy and its potential for device applications in “dilute nitride, in: M. Henini (Ed.), Semiconductors, Elsevier Ltd, 2005.

[10] K.L. Lew, S.F. Yoon, H. Wang, S. Wicaksono, J.A. Gupta, S.P. McAlister, High-gain low turn-on voltage AlGaAs/GaAsNSb/GaAs heterojunction bipolar transistors grown by molecular beam epitaxy, Electron Device Lett. Electron Device Lett. IEEE 28 (2008) 1083, https://doi.org/10.1109/LED.2007.910000.

[11] B.L. Edwards, B. Robinson, A. Biswas, J. Hamkins, 2015. IEEE Int. Conf. Sp. Opt. Syst. Appl. 1-8.

[12] E. Benzi, D.C. Troendle, I. Shurmer, M. James, M. Lutzer, S. Kuhlmann, (2016) SpaceOps Conference, (AIAA 2016-2389).

[13] K.H. Tan, S.F. Yoon, W.K. Loke, S. Wicaksono, K.L. Lew, A. Stohr, O. Ecin, A. Poloczek, A. Malcoci, D. Jager, High-speed picosecond pulse response GaNAsSb photodetectors grown by rf plasma-assisted nitrogen molecular beam epitaxy, Appl. Phys. Lett. 90 (2007) 183515. https://doi.org/10.1063/1.2730585.

[14] W.K. Loke, S.F. Yoon, Z. Xu, K.H. Tan, T.K. Ng, Y.K. Sim, S. Wicaksono, N. Saadsaoud, D. Decoster, J. Chazelas, GaNAsSb/GaAs waveguide photodetector with response up to grown by molecular beam epitaxy, Appl. Phys. Lett. 93 (2008) 081102, https://doi.org/10.1063/1.2976124.

[15] K.H. Tan, S.F. Yoon, W.K. Loke, S. Wicaksono, C. Tripon-Canseliet, S. Faci, N. Saadsaoud, J.F. Lampin, D. Decoster, J. Chazelas, GaNAsSb material for ultrafast microwave photoconductive switching, Appl. Phys. Lett. 93 (2008) 063509, https://doi.org/10.1063/1.2971204.

[16] K.H. Tan, S.F. Yoon, S. Wicaksono, W.K. Loke, D. Li, N. Saadsaoud, C. Tripon-Canseliet, J.F. Lampin, D. Decoster, J. Chazelas, Low temperature grown GaNAsSb: a promising material for photoconductive switch application, Appl. Phys. Lett. 103 (2013) 111113, https://doi.org/10.1063/1.4820797.

[17] A. Maros, N. Faleev, S.H. Lee, J.S. Kim, C.B. Honsberg, R.R. King, “1-eV GaNAsSb for Multijunction Solar Cells”, Proc. 43rd IEEE-PVSC (2016).

[18] I. García, M. Ochoa, I. Lombardero, L. Cifuentes, M. Hinojosa, P. Caño, I. Rey-Stolle, C. Algora, A. Johnson, I. Davies, K.H. Tan, W.K. Loke, S. Wicaksono, S. F. Yoon, Degradation of subcells and tunnel junctions during growth of GaInP/Ga(In)As/GaNAsSb/Ge 4-junction solar cells, Prog. Photovolt. Res. Appl. 25 (2017) 887–895, https://doi.org/10.1002/pip.2930.

[19] V. Polojärvi, A. Aho, A. Tukiainen, A. Schramm, M. Guina, Comparative study of defect levels in GaInNAs, GaNAsSb, and GaInNAsSb for high-efficiency solar cells, Appl. Phys. Lett. 108 (2016) 122104, https://doi.org/10.1063/1.4944844.

[20] N.L. Yurong, K.H. Tan, W.K. Loke, S. Wicaksono, D. Li, S.F. Yoon, P. Sharma, T. Milakovich, M.T. Bulsara, E.A. Fitzgerald, Performance of 1 eV GaNAsSb-based photovoltaic cell on Si substrate at different growth temperatures, Prog. Photovolt. Res. Appl. 25 (2017) 327–332, https://doi.org/10.1002/pip.2870.

[21] F. Dimroth, C. Baur, A.W. Bett, K. Volz, W. Stolz, Comparison of dilute nitride growth on a single- and 8 × 4-inch multiwafer MOVPE system for solar cell applications, J. Cryst. Growth 272 (2004) 726–731, https://doi.org/10.1016/j.jcrysgro.2004.08.038.

[22] B. Sciana, D. Pucicki, D. Radziewicz, J. Serafinczuk, J. Kozlowski, B. Paszkiewicz, M. Tlaczala, P. Poloczek, G. Sek, J. Misiewicz, APMOVPE growth and characterisation of undoped GaAsN/GaAs heterostructures, Vacuum 82 (2008) 377–382, https://doi.org/10.1016/j.vacuum.2007.08.005.

[23] S. Wicaksono, S.F. Yoon, K.H. Tan, W.K. Cheah, Concomitant incorporation of antimony and nitrogen in GaAsSbN lattice-matched to GaAs, J. Cryst. Growth 274 (2005) 355–361, https://doi.org/10.1016/j.jcrysgro.2004.10.050.

[24] N. Miyashita, N. Ahsan, Y. Okada, Generation and collection of photocarriers in dilute nitride GaInNAsSb solar cells, Prog. Photo. Res. Appl. 24 (2016) 28–37, https://doi.org/10.1002/pip.2641.

[25] M. Guina, S. Wang, A. Aho, Molecular beam epitaxy of dilute nitride optoelectronic devices in “molecular beam epitaxy: from research to mass production” 2018. 73–94, Elsevier. ISBN 978-012812136-8, 978-012812137-5. https://doi.org/10.1016/B978-0-12-812136-8.00005-0.

[26] N. Miyashita, Y. Okada, Inverted lattice-matched GaInP/GaAs/GaInNAsSb triple-junction solar cells: Epitaxial lift-off thin-film devices and potential space applications in “Photovoltaics For Space. Key Issues, Missions, and Alternative Technologies” (2023) 265-291, Elsevier ISBN 978-0-12-823300-9. ⟨https://doi.org/10.1016/B978-0-12-823300-9.00013-3⟩.

[27] R.R. King, D.C. Law, C.M. Fetzer, R.A. Sherif, K.M. Edmondson, S. Kurtz, G.S. Kinsey, H.L. Cotal, D.D. Krut, J.H. Ermer, N.H. Karam, Pathways to 40%-efficient concentrator photovoltaics in the 20th European Photovoltaic Solar Energy Conference and Exhibition, Barcelona, Spain, 2005.

[28] A.D. Johnson, K. Nunna, A. Clark, A. Joel, R. Pelzel, Long wavelength dilute nitride VCSELs, edge emitters and detectors for 3D sensing applications, Proceedings of the SPIE OPTO, PC12439, p. PC124390A, San Francisco, USA, 2023. https://doi.org/10.1117/12.2668691.
[29] V. Sabnis, H. Yuen, M. Wiemer, High-efficiency multijunction solar cells employing dilute nitrides, In: Proceedings of the 8th International Conference on Concentrating Photovoltaic Systems, Toledo, Spain (2012). https://doi.org/10.1063/1.4753823.
[30] R. Karim, A. Rahman, J. Akhtar, M. Istiaque Reja, Design and Performance Analysis of GaInNAsSb/GaAs MQW VCSEL Operating at 1550 nm, In: Proceedings of the 3rd International Conference on Electrical Information and Communication Technology (EICT), Khulna, Bangladesh (2017).
[31] S. Kurtz, J. Webb, L. Gedvilas, D. Friedman, J. Geisz, J. Olson, R. King, D. Joslin, N. Karam, Structural changes during annealing of GaInAsN, Appl. Phys. Lett. 78 (2001) 748–750, https://doi.org/10.1063/1.1345819.
[32] K.M. Kim, J. Leeb, J.H. Ryu, Thermal annealing effect on nitrogen related defects of GaInNAs semiconductors, J. Ceram. Process. Res. 16 (2015) 45–48 (https://doi.org/).
[33] N. Miyashita, N. Ahsan, Y. Okada, Improvement of 1.0 eV GaInNAsSb solar cell performance upon optimal annealing, Phys. Status Solidi A 214 (2017) 1600586, https://doi.org/10.1002/pssa.201600586.
[34] M.C. López-Escalante, B. Sciana, W. Dawidowski, K. Bielak, M. Gabás, Atomic configurations in AP-MOVPE grown lattice-mismatched InGaAsN films unravelled by X-ray photoelectron spectroscopy combined with bulk and surface characterization techniques, Appl. Surf. Sci. 433 (2018) 1–9, https://doi.org/10.1016/j.apsusc.2017.10.032.
[35] X.Z. Chen, D.H. Zhang, Y.J. Jin, J.H. Li, J.H. Teng, N. Yakovlev, Effect of rapid thermal annealing on behavior of nitrogen in GaAsN alloys, J. Cryst. Growth 362 (2013) 197–201, https://doi.org/10.1016/j.jcrysgro.2012.03.059.
[36] S.R. Bank, H.B. Yuen, H. Bae, M.A. Wistey, J.S. Harris Jr., Overannealing effects in GaInNAs(Sb) alloys and their importance to laser applications, Appl. Phys. Lett. 88 (2006) 221115, https://doi.org/10.1063/1.2208375.
[37] K. Volz, D. Lackner, I. Németh, B. Kunert, W. Stolz, C. Baur, F. Dimroth, A.W. Bett, Optimization of annealing conditions of (GaIn)(NAs) for solar cell applications, J. Cryst. Growth 310 (2008) 2222–2228, https://doi.org/10.1016/j.jcrysgro.2007.11.199.
[38] T.J. Garrod, J. Kirch, P. Dudley, S. Kim, L.J. Mawst, T.F. Kuech, Narrow band gap GaInNAsSb material grown by metal organic vapor phase epitaxy (MOVPE) for solar cell applications, J. Cryst. Growth 315 (2011) 68–73, https://doi.org/10.1016/j.jcrysgro.2010.08.010.
[39] N. Miyashita, Y. He, N. Ahsan, T. Agui, H. Juso, T. Takamoto, Y. Okada, Incorporation of hydrogen into MBE-grown dilute nitride GaInNAsSb layers in a MOCVD growth ambient, Sol. Energy Mater. Sol. Cells 185 (2018) 359–363, https://doi.org/10.1016/j.solmat.2018.05.043.
[40] R. Kudrawiec, H.B. Yuen, S.R. Bank, H.P. Bae, M.A. Wistey, J.S. Harris, M. Motyka, J. Misiewicz, Fermi level shift in quantum wells GaInNAsSb/GaAs upon annealing studied by contactless electroreflectance, Appl. Phys. Lett. 90 (2007) 061902, https://doi.org/10.1063/1.2437729.
[41] M. Baranowski, R. Kudrawiec, M. Latkowska, M. Syperek, J. Misiewicz, T. Sarmiento, J.S. Harris, Enhancement of photoluminescence from GaInNAsSb quantum wells upon annealing: improvement of material quality and carrier collection by the quantum well, J. Phys. Condens. Matter 25 (2013) 065801, https://doi.org/10.1088/0953-8984/25/6/065801.
[42] M. Albrecht, V. Grillo, T. Remmele, H.P. Strunk, A. Yu. Egorov, Gh Dumitras, H. Riechert, A. Kaschner, R. Heitz, A. Hoffmann, Effect of annealing on the In and N distribution in InGaAsN quantum wells, Appl. Phys. Lett. 81 (2002) 2719–2721, https://doi.org/10.1063/1.1509122.
[43] K. Volz, T. Torunski, O. Rubel, W. Stolz, Direct structural evidence of the change in N-III bonding in (GaIn)(NAs) before and after thermal annealing, J. Appl. Phys. 104 (2008) 053504, https://doi.org/10.1063/1.2970162.
[44] K. Müller, M. Schowalter, A. Rosenauer, D. Hu, D.M. Schaadt, P. Gilet, O. Rubel, R. Fritz, K. Volz, Atomic scale annealing effects on $In_xGa_{1-x}N_yAs_{1-y}$ studied by TEM three-beam imaging, Phys. Rev. B 84 (2011) 045316, https://doi.org/10.1103/PhysRevB.84.045316.
[45] A. Navarro, O. Martinez, B. Galiana, I. Lombardero, M. Ochoa, I. García, M. Gabás, C. Ballesteros, J. Jimenez, C. Algora, Cathodoluminescence characterization of dilute nitride GaNSbAs alloys, J. Electron. Mater. 47 (2018) 5061–5067, https://doi.org/10.1007/s11664-018-6325-3.
[46] N. Miyashita, S. Ichikawa, Y. Okada, Improvement of GaInNAsSb films fabricated by atomic hydrogen-assisted molecular beam epitaxy, J. Cryst. Growth 311 (2009) 3249, https://doi.org/10.1016/j.jcrysgro.2009.03.024.
[47] N. Miyashita, N. Ahsan, Y. Okada, Effect of antimony on uniform incorporation of nitrogen atoms in GaInNAs films for solar cell application, Sol. Energy Mater. Sol. Cells 111 (2013) 127, https://doi.org/10.1016/j.solmat.2012.12.036.
[48] N. Miyashita, Y. He, T. Agui, H. Juso, T. Takamoto, Y. Okada, Inverted lattice-matched triple junction solar cells with 1.0 eV GaInNAsSb subcell by MOCVD/MBE hybrid, Growth J. Photovolt. 9 (2019) 666–672, https://doi.org/10.1109/JPHOTOV.2019.2895807.
[49] A. Aho, R. Isoaho, A. Tukiainen, G. Gori, R. Campesato, M. Guina, Dilute nitride triple junction solar cells for space applications: progress towards highest AM0 efficiency, Prog. Photovolt. Res. Appl. 26 (2018) 740–744, https://doi.org/10.1002/pip.3011.
[50] N. Miyashita, N. Ahsan, M.M. Islam, Y. Okada, Composition control of quinary GaInNAsSb alloy grown by molecular beam epitaxy, Phys. Status Solidi C. 10 (2013) 1369–1372, https://doi.org/10.1002/pssc.201300283.
[51] D.B. Williams, C.B. Carter, "Transmission Electron Microscopy: A Textbook for. Materials Science,", 2nd ed., Springer, New York, 2009.
[52] T. Ahlgren, E. Vainonen-Ahlgren, J. Likonen, W. Li, M. Pessa, Concentration of interstitial and sustitutional nitrogen in GaNxAs1-x, Appl. Phys. Lett. 80 (2002) 2314–2316, https://doi.org/10.1063/1.1465522.
[53] P. Krispin, S.G. Spruytte, J.S. Harris, K.H. Ploog, Electron traps in Ga(As,N) layers grown by molecular-beam epitaxy, Appl. Phys. Lett. 80 (2002) 2120–2122, https://doi.org/10.1063/1.1463214.
[54] A. Khan, S.R. Kurtz, S. Prasad, S.W. Johnston, J. Gou, Correlation of nitrogen related traps in InGaAsN with solar cell properties, Appl. Phys. Lett. 90 (2007) 243509, https://doi.org/10.1063/1.2747664.
[55] A. Kosa, L. Stuchlikova, L. Harmatha, M. Mikolasek, J. Kovac, B. Sciana, W. Dawidowski, D. Radziewicz, M. Tlaczala, Defect distribution in InGaAsN/GaAs multilayer solar cells, Sol. Energy 132 (2016) 587–590, https://doi.org/10.1016/j.solener.2016.03.057.